



저작자표시-비영리-변경금지 2.0 대한민국

이용자는 아래의 조건을 따르는 경우에 한하여 자유롭게

- 이 저작물을 복제, 배포, 전송, 전시, 공연 및 방송할 수 있습니다.

다음과 같은 조건을 따라야 합니다:



저작자표시. 귀하는 원저작자를 표시하여야 합니다.



비영리. 귀하는 이 저작물을 영리 목적으로 이용할 수 없습니다.



변경금지. 귀하는 이 저작물을 개작, 변형 또는 가공할 수 없습니다.

- 귀하는, 이 저작물의 재이용이나 배포의 경우, 이 저작물에 적용된 이용허락조건을 명확하게 나타내어야 합니다.
- 저작권자로부터 별도의 허가를 받으면 이러한 조건들은 적용되지 않습니다.

저작권법에 따른 이용자의 권리는 위의 내용에 의하여 영향을 받지 않습니다.

이것은 [이용허락규약\(Legal Code\)](#)을 이해하기 쉽게 요약한 것입니다.

[Disclaimer](#)

공학석사학위논문

리튬이온 배터리 실리콘 음극을 위한
금속 나노와이어 도전재 및 상이 사슬 길이
구조 기반 전도성 고분자 바인더 개발

Designing Conductive Polymer Binders Augmented by
Varying Chain Lengths with Metal Nanowires for Silicon
Anodes in Lithium-Ion Batteries

2022년 2월

서울대학교 대학원

기계공학부

김 재 원

리튬이온 배터리 실리콘 음극을 위한 금속 나노와이어 도전재 및 상이 사슬 길이 구조 기반 전도성 고분자 바인더 개발

Designing Conductive Polymer Binders Augmented by
Varying Chain Lengths with Metal Nanowires for Silicon
Anodes in Lithium-Ion Batteries

지도교수 고 승 환

이 논문을 공학석사 학위논문으로 제출함

2021년 10월

서울대학교 대학원

기계공학부

김 재 원

김재원의 공학석사 학위논문을 인준함

2021년 12월

위 원 장 : _____ 김 민 수 (인)

부위원장 : _____ 고 승 환 (인)

위 원 : _____ 민 경 덕 (인)

Abstract

Silicon (Si) is the most promising anode material for lithium-ion batteries (LIBs) with its high theoretical capacity, but it suffers from huge volume changes during charge/discharge. Conductive polymer can maintain electrical paths to Si and stable electrode structures. Herein, novel polymer composites with a hierarchical structure by different chain lengths are designed and provide densely distributed hydrogen bonding and crosslinking, achieving higher electrical conductivity and stretchability. Further, silver nanowire network that is integrated into Si anodes imparts 3D facile electron transports, void space to buffer the volume changes, and increased adhesion with current collectors. This anode achieves the specific capacity of 1066 mAh g⁻¹ with the current density of 0.8 A g⁻¹ after 100 cycles. Its superior volume buffering performance and facilitated charge transfer are further confirmed by SEM and EIS, respectively.

Keyword : Lithium-ion batteries, Silicon anodes, Conductive binder, Hierarchical structure, Silver nanowires

Student Number : 2020-27003

Table of contents

Chapter 1. Introduction	6
1.1 Backgrounds and previous studies	6
1.2 The objective of this study.....	8
Chapter 2. Method	10
2.1 Materials	10
2.2 The fabrication of the 5-P binder	10
2.3 The synthesis of AgNWs	11
2.4 The fabrication of anodes and coin cells	11
2.5 Characterizations	12
Chapter 3. Binder characterizations	14
3.1 Material characterizations.....	14
3.2 The effect of the hierarchical structure.....	17
Chapter 4. Anode characterizations	21
4.1 Material characterizations.....	21
4.2 Rigidity test.....	22
4.3 Half-cell test.....	23
Chapter 5. Conclusion.....	28
5.1 Summary of this work	28
5.2 Future work.....	28
Reference.....	30
Abstract in Korean.....	33

List of figures

Figure 1. The schematic diagrams of main mechanisms for drastic capacity fade and short cycle life of Si anodes; (a) Pulverization and (b) delamination.

Figure 2. (a) The schematic diagram of polymer constituents of the 5-P binder. (b) The schematic diagram of Si/5-P/AgNW electrode during lithiation and delithiation.

Figure 3. (a) The schematic diagram of the fabrication process and (b) an optic image of a free-standing conductive polymer film.

Figure 4. The schematic diagram of the fabrication process of Si/5-P/AgNW electrode.

Figure 5. Raman spectra of PEDOT:PSS (PP), PP/PEG/PEO, and the 5-P binder.

Figure 6. Topography and phase images of PP and the 5-P binder. The scale bars are 200 nm.

Figure 7. (a) X-ray diffraction of the 5-P binder before and after the annealing process at 140 °C for 6 h. (b) The schematic diagram of chemical crosslinking between PSS and PEG/PEO through the condensation reaction.

Figure 8. X-ray diffraction of PP/PEG/PEO before and after the annealing process

at 140 °C for 6 h.

Figure 9. The schematic diagram of the hierarchical structure of the 5-P binder by PEG and PEO that have the same monomer unit but different chain lengths.

Figure 10. Electrical conductivity with respect to varying PEG and PEO wt% for (a) PP and (b) PP/PVA.

Figure 11. Electrical conductivity of PP, PP/PVA, and the 5-P binder.

Figure 12. Stress-strain behaviors of the 5-P binder, PP/PVA/PEG, and PP/PVA/PEO.

Figure 13. TGA curve of the 5-P binder, PP/PVA/PEG, and PP/PVA/PEO. The inset is a TGA curve for a shorter temperature range.

Figure 14. (a) SEM image and (b) EDS images of Si/5-P/AgNW electrode. The scale bars of (a) and (b) are 1 μm and 200 nm, respectively.

Figure 15. FT-IR spectroscopy of Si/5-P, Si/5-P/AgNW electrodes, and AgNW.

Figure 16. (a) Peeling test with 3M tapes on the electrode for Si/5-P/AgNW, Si/5-P, and Si/CMC electrode. (b) Optic images of Si/5-P/AgNW electrodes with successive folding and unfolding. The scale bars are 5 mm.

Figure 17. CV curves of Si/5-P/AgNW electrode.

Figure 18. Charge-discharge voltage curves at 1st, 5th, and 10th cycles under the current density of 0.8 A g^{-1} of (a) Si/5-P/AgNW, (b) Si/5-P, and (c) Si/CMC electrodes.

Figure 19. a) Cycling performance and (b) discharge capacity after 100 cycles at 0.8 A g^{-1} of different electrodes. (c) Cycle test of Si/5-P/AgNW electrode at 0.1 A g^{-1} . (d) Rate capability at 0.1, 0.2, 0.4, 0.8, and 1.6 A g^{-1} of different electrodes.

Figure 20. Nyquist plots of different electrodes after 20 cycles of charge/discharge. The inset is an equivalent circuit model.

Figure 21. SEM images of the electrode surface (a-c) before and (d-e) after charge/discharge cycles. (a), (d) Si/5-P/AgNW, (b), (e) Si/5-P, and (c), (f) Si/CMC electrodes. The scale bars are $10 \text{ }\mu\text{m}$.

Chapter 1. Introduction

1.1. Backgrounds and previous studies

As the climate changes and accompanying problems have been considered forthcoming crises, various approaches to resolving them such as renewable electricity have been conducted.^{1, 2} One of the feasible and effective ways is the electrification of every single device including, particularly, vehicles.^{3, 4} To stably power vehicles as efficiently as internal combustion engines (ICE) does, lithium-ion batteries (LIBs) are a promising candidate and have been being world-widely employed.⁵⁻⁷ However, low energy density and short life cycle of LIBs are still huge obstacles to replacing ICE.

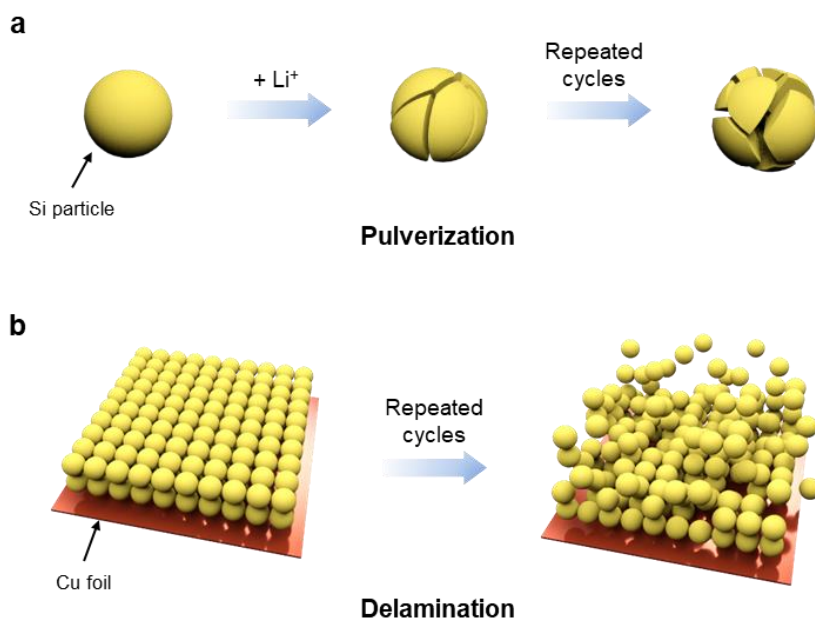


Figure 1. The schematic diagrams of main mechanisms for drastic capacity fade and short cycle life of Si anodes; (a) Pulverization and (b) delamination.

As one of the solutions to manufacture high-performance LIBs, new anode

materials such as silicon (Si) and lithium metal have been examined as alternatives of conventional graphite. Particularly, Si that provides ten times higher theoretical capacity density (4200 mAh g^{-1}) than graphite does (372 mAh g^{-1}) is considered the most feasible anode material in the near future.^{8,9} However, huge volume changes of Si during lithiation and delithiation, which are a common dilemma of active materials that forms alloys with lithium (Li), lead to pulverized Si and low cycling performance of Si anodes (**Figure 1**).¹⁰ To overcome this challenge, various nano-materials such as nanowires, nanosheets, and buffer layers with high porosity have been investigated.¹¹⁻¹³ Nevertheless, complicated fabrication processes have deterred the commercialization of Si anodes.

Polymer binders help to fixate electrode materials and affect electrochemical performance as well as mechanical stability.¹⁴ For Si anodes, polyvinylidene fluoride (PVDF) binder, which is being conventionally used in the market, shows weak Van der Waals interaction and less stable adhesion to current collectors.¹⁵ Therefore, polymer binders that are soluble in water, such as CMC,¹⁵ alginate,¹⁶ and PAA¹⁷ have been employed in Si anodes. Although these binder materials have shown robust electrode structure and enhanced cycle life, electrically disconnected Si that is unable to form alloys with Li necessarily occurs.¹⁸

To provide a steady electrical connection to Si, conducting polymers have been widely studied, enabling Si particles to have continuous electrical paths, thus, reversibly form alloys with Li under severe volume variances.^{19, 20} Poly(3,4-ethylenedioxythiophene):poly(styrene sulfonate) (PEDOT:PSS) is able to obtain high electrical conductivity ($> 100 \text{ S cm}^{-1}$) by doping with various polar materials and be easily processed with other water-soluble materials.^{21, 22} It is reported that PEDOT:PSS was treated with polymers with functional groups such as hydroxyl

and carboxyl groups and used as binder materials, improving the rigidity of electrodes and ionic transportation.^{23, 24} Nonetheless, additional components as secondary dopants including polar solvent and acid solution were added, requiring the evaporation process at high temperature.

Metal nanowires that can be synthesized in a one-pot, such as copper nanowires (CuNWs) and silver nanowires (AgNWs), have a high aspect ratio (~1000), thereby showing exceptional electrical conductivity with only a small amount.^{25, 26} Current collectors made of CuNWs were used for Si and Li metal anodes, providing enough void space and achieving much higher gravimetric capacity.^{27, 28} Recently, sandwich-structured 2d AgNW layers were introduced to Si anodes, displaying enhanced initial Coulombic efficiency and specific capacity.²⁹

1.2. The objective of this study

Herein, PEDOT:PSS/PVA is integrated with chain length-varying PEG/PEO (5-P binder), realizing electron-ion conductive binders with enhanced mechanical properties (**Figure 2a**). PEG/PEO has the same monomer of ether groups but different molecular weights and acts as second dopants to PEDOT:PSS to increase the electrical conductivity of the binder. They further provide dense hydrogen bonding and crosslinking sites, improving the strength and stretchability of the 5-P binder. Additionally, the entangled network of AgNWs provides superior 3D electrical path, buffer space to accommodate the volume changes, and higher adhesive force to current collectors. With these enhancements, Si/5-P/AgNW electrode can endure huge volume changes during lithiation and delithiation with continuous electron paths maintained through the 5-P binder and AgNW network

(Figure 2b).

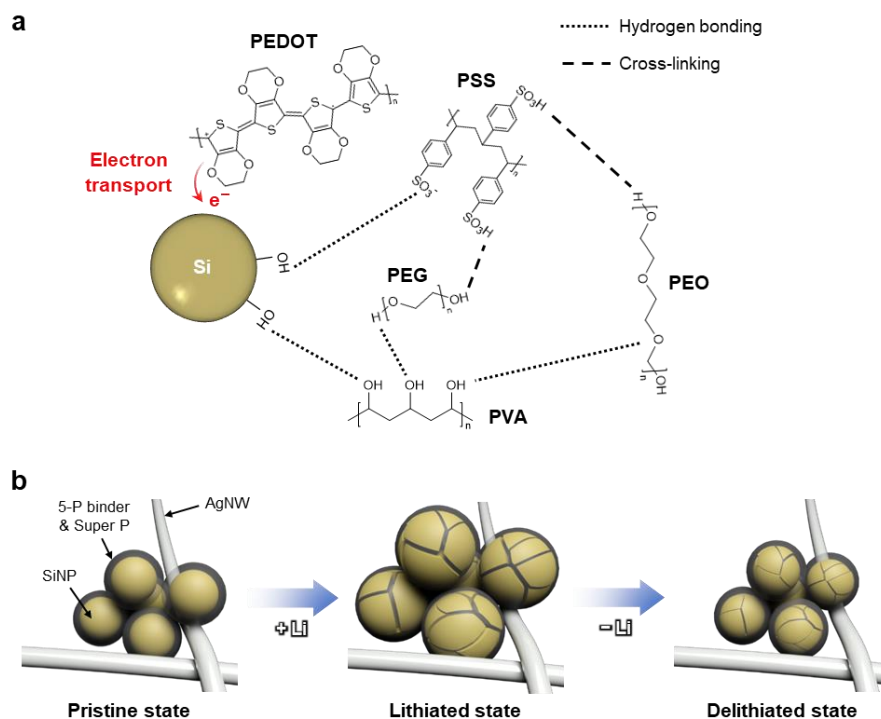


Figure 2. (a) The schematic diagram of polymer constituents of the 5-P binder. (b) The schematic diagram of Si/5-P/AgNW electrode during lithiation and delithiation.

Chapter 2. Method

2.1. Materials

PEDOT:PSS solution (Cleovis PH 1000) was bought from Heraeus. PVA ($M_w = 89000-98000$), PEG ($M_w = 8000$), PEO ($M_w = 600000$), AgNO_3 (99.8%), FeCl_3 (97%), polyvinylpyrrolidone (PVP) ($M_w = 360000$) were purchased from Sigma Aldrich. Additionally, ethylene glycol (EG) (99%) from Alfar Aesar and Super P from MTI were used.

2.2. The fabrication of the 5-P binder

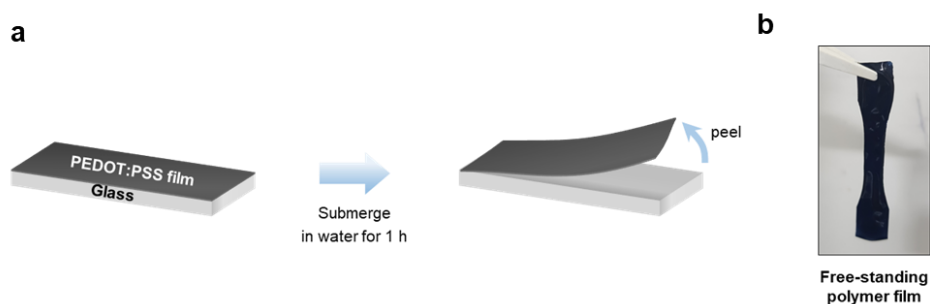


Figure 3. (a) The schematic diagram of the fabrication process and (b) an optic image of a free-standing conductive polymer film.

To prepare the 5-P binder, 10.4 mg of PVA, 5.2 mg of PEG, and 5.2 mg of PEO were added to 1 mL of PEDOT:PSS solution and stirred at 90 °C for 2 h and at 25 °C for 8 h sequentially. For fabricating the free-standing polymer film for the tensile test, 0.5 mL of the 5-P binder solution was deposited on a glass substrate and thermally treated on the hot plate with the sequence of 50 °C for 1 h, 90 °C for

2 h, and 140 °C for 6 h to remove bubbles in the solution. Then, it was submerged into deionized water (DI) for 1 h and carefully peeled off (**Figure 3**).

2.3. The synthesis of AgNWs

AgNWs were synthesized via a modified polyol method as reported in previous research.³⁰ 0.8 g of PVP and 1 g of AgNO₃ were dissolved into 100 mL of EG. Then, 360 µL of EG containing 20 mM of FeCl₃ was added to the solution. After the solution in the beaker was immersed into the oil bath and heated at 130 °C for 5 h, it was cleaned with acetone and centrifuged three times, redispersed in DI. The density of resultant AgNW solutions is 12 mg mL⁻¹.

2.4. The fabrication of anodes and coin cells

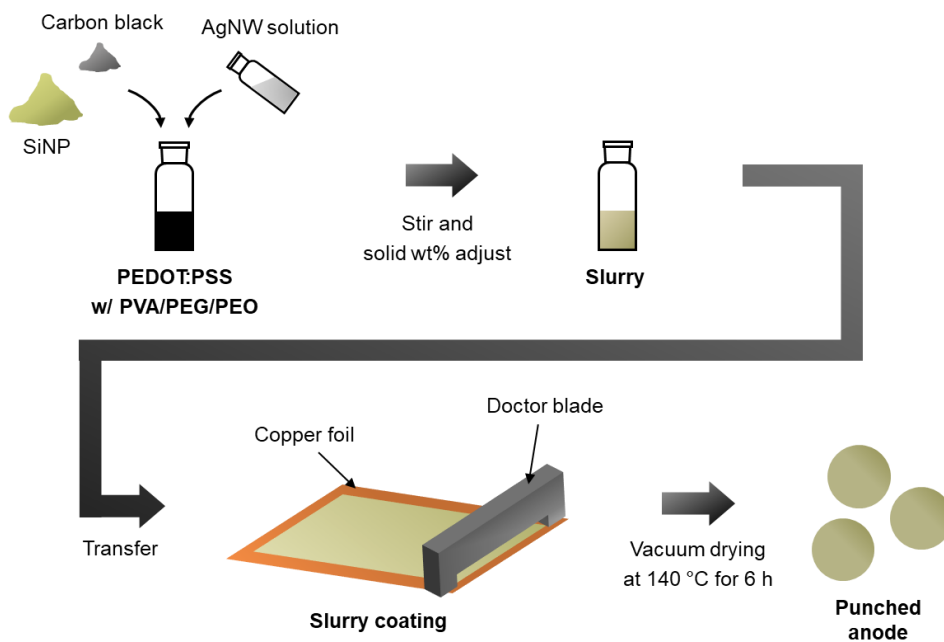


Figure 4. The schematic diagram of the fabrication process of Si/5-P/AgNW electrode.

For fabricating Si/5-P/AgNW electrode, 60 mg of SiNP, 0.5 mL of the AgNW solution, and 6 mg of Super P were added into 1 mL of the 5-P binder and stirred for 8 h, and then the solid/liquid wt% of the slurry was properly adjusted. After the slurry was doctor-bladed on the copper foil, it was dried at 140 °C for 6 h in a vacuum oven (**Figure 4**). For comparison, the Si/5-P electrode was fabricated with 60 mg of SiNP and 12 mg of Super P for 1 mL of the 5-P binder solution. Conventional Si/CMC electrode was made with a weight ratio of SiNP:CMC:Super P=6:3:1. These electrodes were assembled into the 2032 cells for half-cell test in the glove box filled with argon (Ar) gas, where the ratio of O₂ and H₂O in the atmosphere is lowered than 1 ppm, respectively. Li foil counter electrode, Celgard 2400 separator, and electrolytes that consist of 1M LiPF₆ in ethylene carbonate (EC)/diethylene carbonate (DEC) (1:1 by vol) with 10 wt% of fluoroethylene carbonate (FEC) were used for the coin cell fabrication.

2.5. Characterizations

Bonding structures of polymer composites were characterized by Raman spectroscopy (inVia, Renishaw). Topology characterization and phase imaging were performed using AFM (NX-10, Park Systems). XRD for the crystallinity analysis was conducted by D8 Advance, Bruker. Electrical conductivities (σ) of polymer composite thin films were evaluated based on the equation below

$$\sigma = (R_{sh} \times t)^{-1}$$

Where R_{sh} and t are the sheet resistance and the thickness of polymer film, respectively. Sheet resistances and thicknesses were measured using a four-point probe (M4P302, MSTECH) and a contact surface profiler (ET200, KOSAKA),

respectively. Tensile test and peeling test were conducted on a universal tensile machine (Instron 5948). Morphology and elements of Si anodes were characterized with a field emission scanning electron microscope (JSM-7800F Prime, JEOL Ltd). Bonding structures of anodes and AgNWs were verified by Fourier-transform infrared (FT-IR) spectroscopy (Nicolet IS50, Thermo Fisher Scientific). Cyclic voltammetry (CV) was conducted with the scan rate of 0.1 mV s^{-1} for the voltage range of 0.01-1.2 V. Galvanostatic discharge/charge between 0.01 and 1.2 V was performed for measuring cycling performance and rate capability of anodes. Electrochemical impedance spectroscopy (EIS) was conducted within the frequency of 10 mHz to 100 kHz with the amplitude of 10 mV. All electrochemical characterizations were performed using WBCS3000 (WonAtech, Korea).

Chapter 3. Binder characterizations

3.1. Material characterizations

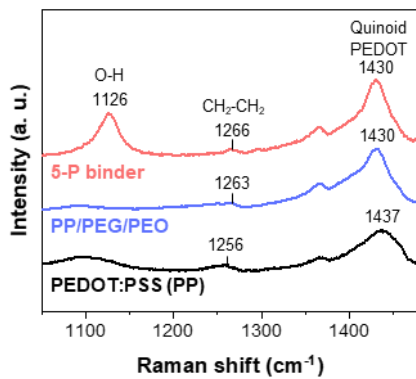


Figure 5. Raman spectra of PEDOT:PSS (PP), PP/PEG/PEO, and the 5-P binder.

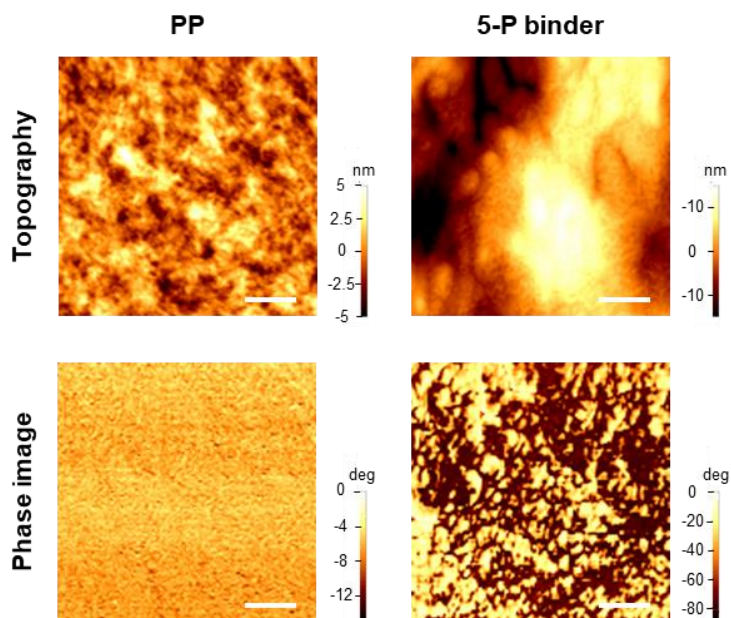


Figure 6. Topography and phase images of PP and the 5-P binder. The scale bars are 200 nm.

The 5-P binder is prepared by simply mixing PEG, PEO, and PVA into PEDOT:PSS (PP) solution. Firstly, Raman spectra of PP, PP/PEG/PEO, and the 5-P binder are measured for validating changes of bonding structures along with the addition of various polymers (**Figure 5**). The C=C symmetrical stretching at $\sim 1440\text{ cm}^{-1}$ of PEDOT shows a prominent peak for all binders.³¹ It has to be noted that this peak is narrowed and red-shifted for the 5-P binder and PP/PEG/PEO, indicating PEDOT chain structure changes from the benzoid structure to the quinoid structure that is more preferred for interconnected linear PEDOT chains.³² Meanwhile, the CH₂-CH₂ twisting of PEG/PEO blue-shifts the peak at $\sim 1250\text{ cm}^{-1}$, and the O-H vibration displays a noticeable peak at 1126 cm^{-1} , showing they form stable polymer composites.^{33, 34} Further, we analyze phase changes and topology of polymer composites using atomic force microscopy (AFM) as shown in **Figure 6**. For PP, small grain sizes that are known to have higher energy barriers for electron transports and almost no phase separation between PEDOT and PSS are observed. However, the 5-P binder displays larger grain sizes and obvious phase separation, leading to forming interconnected PEDOT chains and thus imparting enhanced electrical conductivity.

Moreover, to examine the crosslinking between PSS and PEG/PEO that is expected to improve the mechanical stability of the 5-P binder, X-ray diffraction (XRD) of the 5-P binder is measured and shown in **Figure 7a**. The characteristic crystalline peak of PEG/PEO at 19° vanished after thermal treatment at 140°C for 6 h as a result of the crosslinking through the condensation reaction between PSS and PEG/PEO that decreased the crystallinity (**Figure 7b**).^{23, 35} The characteristic peaks of PVA at $\sim 20^\circ$ are inherently wide so that the 5-P binder show rather gradual changes of the peak. With no PVA added into the binder, the polymer

binder indicates prominent peak changes after the annealing (**Figure 8**).

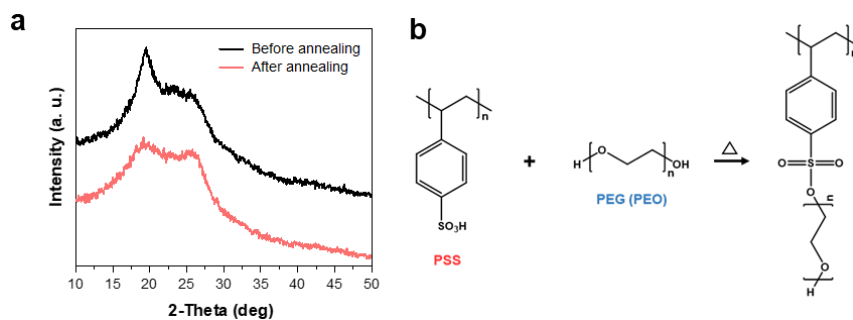


Figure 7. (a) X-ray diffraction of the 5-P binder before and after the annealing process at 140 °C for 6 h. (b) The schematic diagram of chemical crosslinking between PSS and PEG/PEO through the condensation reaction.

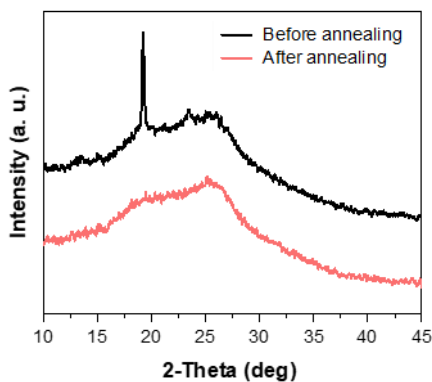


Figure 8. X-ray diffraction of PP/PEG/PEO before and after the annealing process at 140 °C for 6 h.

3.2. The effect of the hierarchical structure

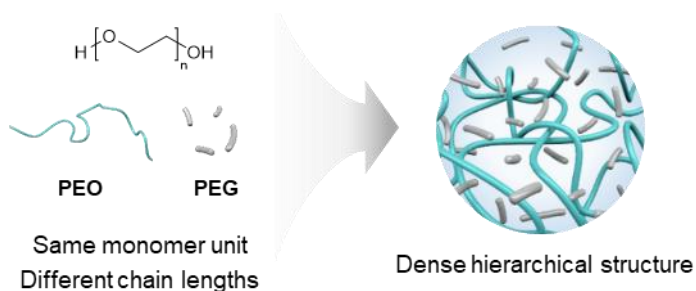


Figure 9. The schematic diagram of the hierarchical structure of the 5-P binder by PEG and PEO that have the same monomer unit but different chain lengths.

PEG and PEO have the same monomer, but the chain length of PEO is about 1,000 times longer than that of PEG. Therefore, they could build hierarchical structures, where PEO forms a large frame while PEG is located inside (**Figure 9**). This is able to enhance the screening effect to PP and provide dense hydrogen bonding and crosslinking.

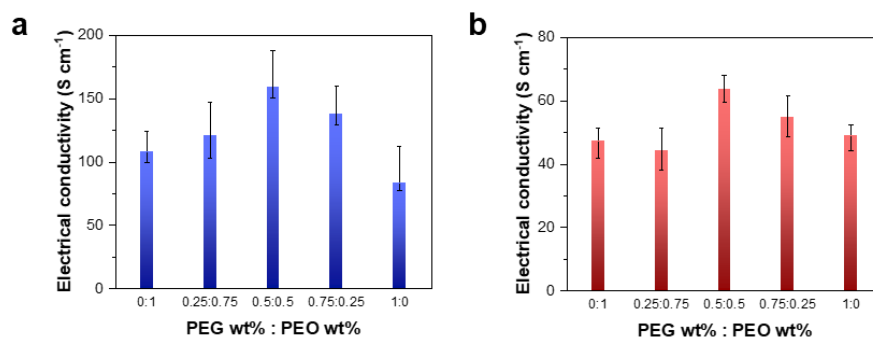


Figure 10. Electrical conductivity with respect to varying PEG and PEO wt% for (a) PP and (b) PP/PVA.

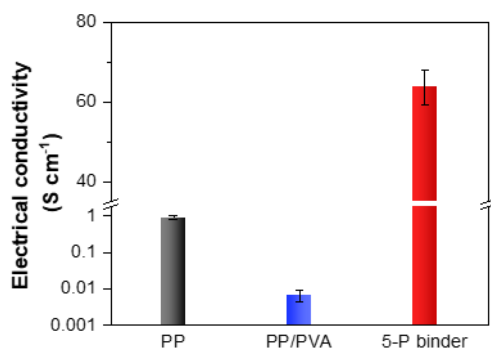


Figure 11. Electrical conductivity of PP, PP/PVA, and the 5-P binder.

Firstly, electrical conductivity of PP polymer film is measured with respect to the amount of PEG/PEO (**Figure 10a**). The polymer composite that is mixed with 0.5 wt% of PEG and 0.5 wt% of PEO in regard to pristine PP solution shows the highest electrical conductivity of 159.1 S cm⁻¹ than PEG only (83.7 S cm⁻¹) and PEO only polymer composites (108 S cm⁻¹). Further, with the addition of 1 wt% of PVA to PP solution, the same tendency of increases in electrical conductivity is observed, as the 5-P binder that retains both PEG and PEO achieved higher conductivity (63.7 S cm⁻¹) than PEG-added polymer (49.1 S cm⁻¹) and PEO-added polymer (47.3 S cm⁻¹) (**Figure 10b**). This phenomenon might be due to intensified screening effect of PEG/PEO to electrostatically attracted PEDOT and PSS, since longer PEO chain might be able to form aligned screens, and shorter PEG chain is expected to more freely flow into the gap between polymer chains. On the other hand, pure PP and PEDOT:PSS/PVA shows the electrical conductivity of 0.9 and 0.006 S cm⁻¹, respectively, demonstrating the coexistence of PEG and PEO highly increased the electrical conductivity of the 5-P binder (**Figure 11**).

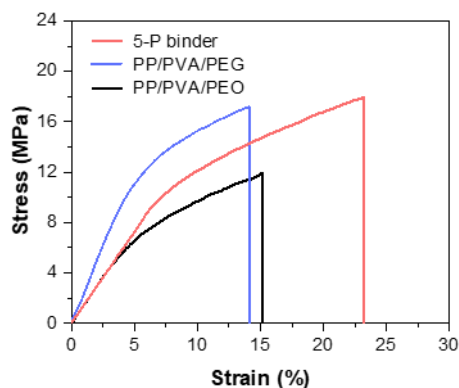


Figure 12. Stress-strain behaviors of the 5-P binder, PP/PVA/PEG, and PP/PVA/PEO.

Further, for characterizing the impact of coexisting PEG and PEO on the mechanical property, the tensile test is conducted with free-standing polymer films as shown in **Figure 12**. PP/PVA/PEG and PP/PVA/PEO show decent elongation at break of 14.2% and 15.1%, respectively, whereas the 5-P binder demonstrates enhanced stretchability (23.3%). It has to be noted that the tensile strength of the 5-P binder (18.0 MPa) is higher than that of PP/PVA/PEG (17.1 MPa) and PP/PVA/PEO (12.0 MPa). These enhancements would be ascribed to homogeneous and dense hydrogen bonding and crosslinking by the hierarchical structures of the 5-P binder. Therefore, the 5-P binder would more effectively endure and accommodate the volumetric expansion, being helpful for the longer cycle life of Si anodes.

Thermal stability, moreover, of polymer composites is also demonstrated via thermal gravimetric analysis (TGA). The 5-P binder, PP/PVA/PEG, and PP/PVA/PEO show similar thermal stability over a temperature range from 100 °C to 600 °C, as displayed in **Figure 13**. Nonetheless, for temperature below 200 °C

where decomposition of battery components including SEI and electrolytes begins and proceeds,³⁶ the 5-P binder demonstrates slightly lower mass loss than PP/PVA/PEG and PP/PVA/PEO, which indicates slightly better thermal endurance of the 5-P binder, probably attributed to hierarchical structures with dense hydrogen bonding and crosslinking.³⁷

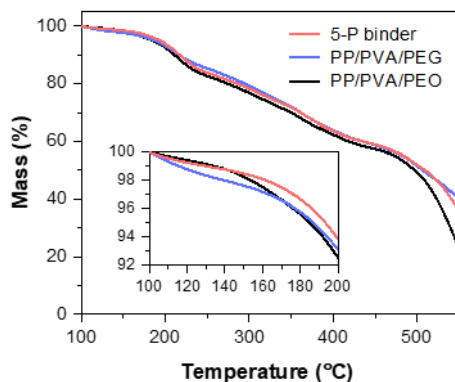


Figure 13. TGA curve of the 5-P binder, PP/PVA/PEG, and PP/PVA/PEO. The inset is a TGA curve for a shorter temperature range.

Chapter 4. Anode characterizations

4.1. Material characterizations

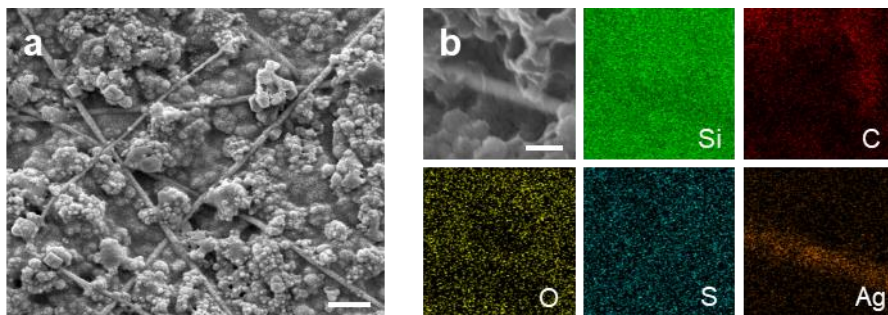


Figure 14. (a) SEM image and (b) EDS images of Si/5-P/AgNW electrode. The scale bars of (a) and (b) are 1 μm and 200 nm, respectively.

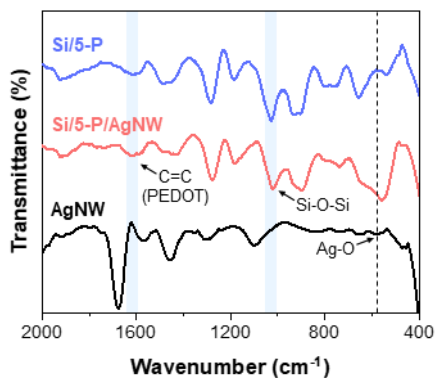


Figure 15. FT-IR spectroscopy of Si/5-P, Si/5-P/AgNW electrodes, and AgNW.

To prepare Si anodes, ~5 wt% of AgNWs with an aspect ratio of ~1000 are added to the 5-P binder solution with SiNP. **Figure 14a,b** are scanning electron microscopy (SEM) and energy dispersive spectroscopy (EDS) images of Si/5-P/AgNW electrode, showing the 5-P binder evenly covers other electrode materials

so that stabilized SEI can be constructed by preventing direct contacts with electrolytes. It is worth noting that even a small amount of AgNWs can form entangled structures, providing superfast 3D electron transports and enough buffer space for large volume changes.

To verify changes of bonding structures by adding SiNPs and AgNWs, Fourier-transform infrared (FT-IR) spectroscopy for Si/5-P electrode, Si/5-P/AgNW electrode, and AgNW is conducted (**Figure 15**). The peak of Si-O-Si bond of SiNP at 1030 cm^{-1} and C=C bond of PEDOT chain at 1635 cm^{-1} are verified for both Si/5-P and Si/5-P/AgNW electrodes.^{38, 39} In contrast, the characteristic peak of Ag-O at 582 cm^{-1} appears only for Si/5-P/AgNW electrode, which shows AgNW network is stably formed in the electrode.⁴⁰

4.2. Rigidity test

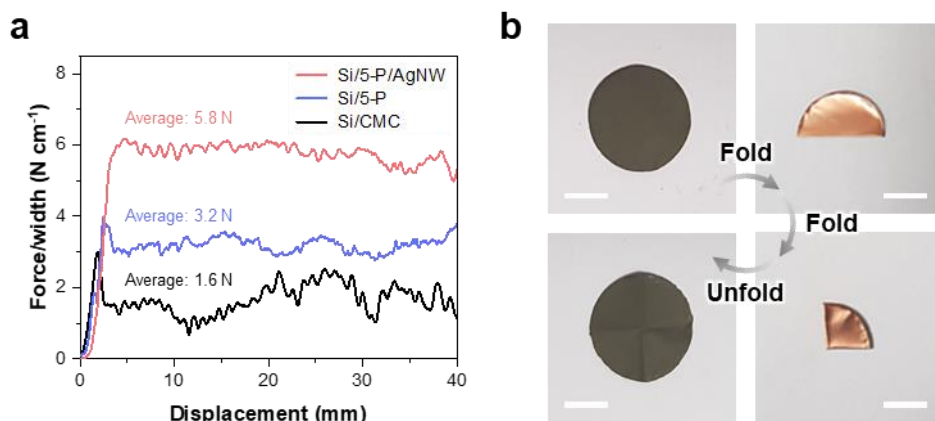


Figure 16. (a) Peeling test with 3M tapes on the electrode for Si/5-P/AgNW, Si/5-P, and Si/CMC electrodes. (b) Optic images of Si/5-P/AgNW electrode with successive folding and unfolding. The scale bars are 5 mm.

For measuring adhesive property of electrodes to the copper foil current collectors,

a 180° peeling test is performed using commercial 3M tapes on the tensile tester (**Figure 16a**). Si/5-P electrode exhibits higher adhesive force (3.2 N) compared to Si/CMC electrode (1.6 N), showing that the 5-P binder provides stronger interaction with the current collector. It has to be noted that Si/5-P/AgNW electrode shows highly enhanced adhesive property (5.8 N). This result is attributed to the entangled AgNW network that rigidly clings to other electrode materials, which requires higher force to detach the electrode materials from the current collector. Therefore, Si/5-P/AgNW electrode can prevent the delamination during charge/discharge and improve the capacity retention. Further, we fold and unfold Si/5-P/AgNW electrode multiple times, but they show no detachment and cracks of the electrode materials, demonstrating the rigidity of the electrode (**Figure 16b**).

4.3. Half-cell test

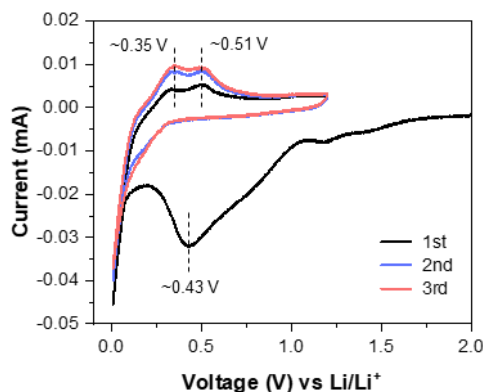


Figure 17. CV curves of Si/5-P/AgNW electrode.

2032 coin cells with Si/5-P/AgNW electrode as a working electrode and lithium foil as a counter electrode are fabricated, and their electrochemical performances

are measured. Firstly, cyclic voltammetry (CV) is conducted for Si/5-P/AgNW electrode (**Figure 17**). For the cycle from 1st and 3rd, cathodic peak at ~ 0.1 V and anodic peak at ~ 0.35 V and ~ 0.51 V are confirmed, which indicates that Si turns into amorphous Li_xSi , and Li_xSi into Si, respectively.⁴¹ Additionally, increases in peak currents as cycles proceed show the activation of Si with stable SEI formed after the first cycle.

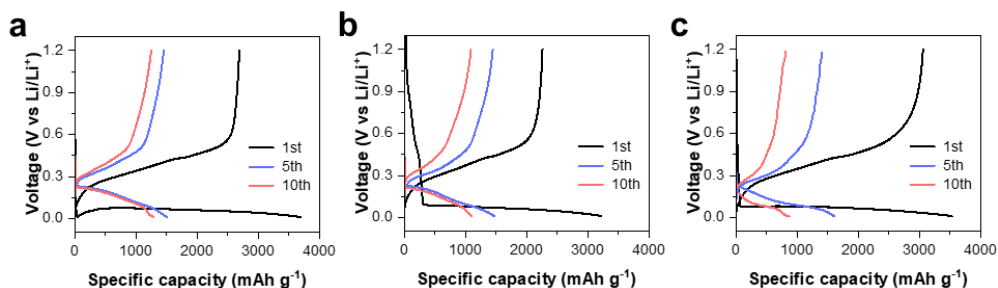


Figure 18. Charge-discharge voltage curves at 1st, 5th, and 10th cycles under the current density of 0.8 A g^{-1} of (a) Si/5-P/AgNW, (b) Si/5-P, and (c) Si/CMC electrodes.

For validating capacity performance, repeated charge/discharge cycles are conducted with the constant current density of 0.8 A g^{-1} up to 100 cycles. Voltage profiles of Si/5-P/AgNW, Si/5-P, and Si/CMC electrodes at 1st, 5th, 10th cycle are presented in **Figure 18**. Stabilized voltage plateaus within 0-0.25 V are found, which shows the formation of Si-Li alloys. Si/5-P/AgNW electrode also shows the initial discharge capacity of 3700 mAh g^{-1} which is higher than that of Si/5-P (3221 mAh g^{-1}) and Si/CMC electrodes (3531 mAh g^{-1}). As shown in **Figure 19a**, Si/5-P/AgNW electrode further demonstrates higher specific capacity of 1066 mAh g^{-1} after 100 cycles, while Si/5-P and Si/CMC electrodes show the specific capacity of 830 and 128 mAh g^{-1} , respectively. Moreover, the rate capability of electrodes is

presented in **Figure 19b**. Si/5-P/AgNW electrode achieves the specific capacity of 3613, 1989, 1581, 1125, and 563 mAh g⁻¹ at the current density of 0.1, 0.2, 0.4, 0.8, and 1.6 A g⁻¹, respectively. On the contrary, Si/5-P and Si/CMC electrodes demonstrate much lower rate capabilities; Si/5-P electrode shows 3016, 1601, 1257, 895, and 536 mAh g⁻¹, and Si/CMC electrode shows 3309, 1387, 660, 281, and 6 mAh g⁻¹ with the current density of 0.1, 0.2, 0.4, 0.8, and 1.6 A g⁻¹, respectively. It has to be noted that for the case of discharging with the current that returns to 0.1 A g⁻¹, Si/5-P/AgNW electrode displays the highest reversible capacity of 1543 mAh g⁻¹. These enhanced specific capacity and long-term cycling performance are attributed to 1) the 5-P binder with the improved electrical and mechanical properties and 2) entangled AgNW network with ultrafast electron transport, sufficient empty spaces, and improved adhesion with the current collector. EIS experiments are conducted with the frequency range from 10 mHz to 100 kHz for the electrodes after 20 cycles of charge/discharge, and their Nyquist plots where semi-circles formed at higher frequency reflect charge transfer resistances are shown in **Figure 20**.⁴² Si/5-P/AgNW electrode exhibits the lowest charge transfer resistance, compared to Si/5-P and Si/CMC electrodes, which would further demonstrate facilitated kinetics of lithiation/delithiation reactions by the combination of the 5-P binder and AgNW network.

To verify buffering ability for volume changes of Si, surfaces of the electrodes before and after cycle test are observed by SEM (**Figure 21**). Whereas the surface of all electrodes is intact before cycles, cracks on Si/CMC and Si/5-P electrode form after 20 cycles of charge/discharge. The crack on Si/5-P electrode is narrower than that on Si/CMC electrode, showing improved buffering function of the 5-P binder for SiNP. Notably, Si/5-P/AgNW electrode shows rare cracks and an almost

intact surface, which demonstrates better mechanical stability of Si/5-P/AgNW electrode under charge/discharge cycles.

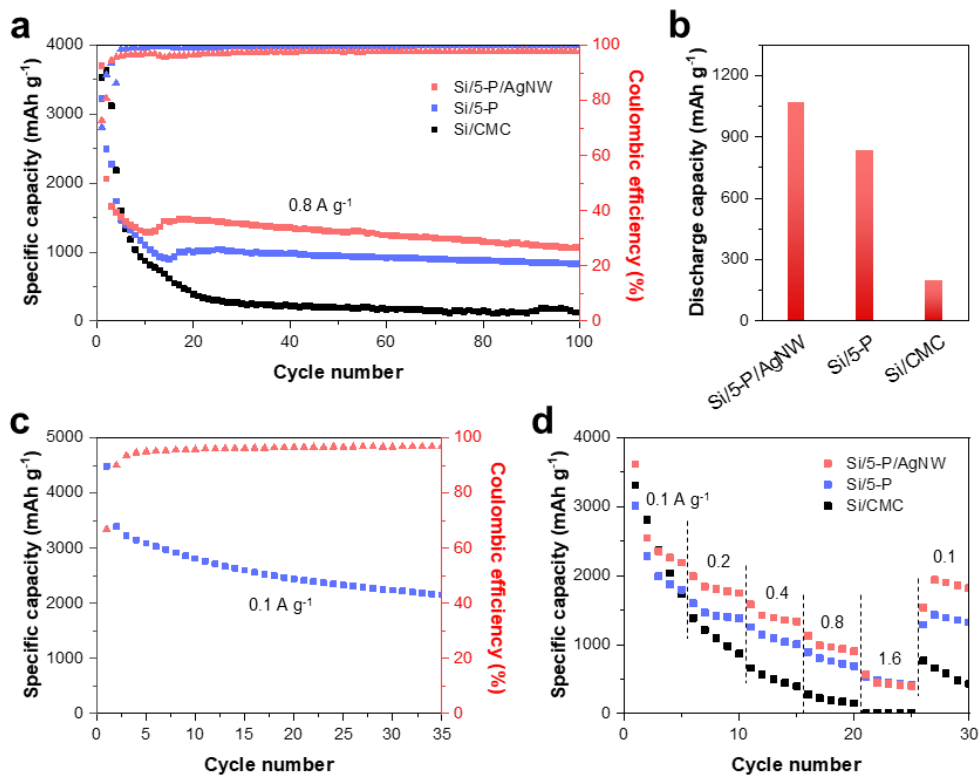


Figure 19. (a) Cycling performance and (b) discharge capacity after 100 cycles at 0.8 A g⁻¹ of different electrodes. (c) Cycle test of Si/5-P/AgNW electrode at 0.1 A g⁻¹. (d) Rate capability at 0.1, 0.2, 0.4, 0.8, and 1.6 A g⁻¹ of different electrodes.

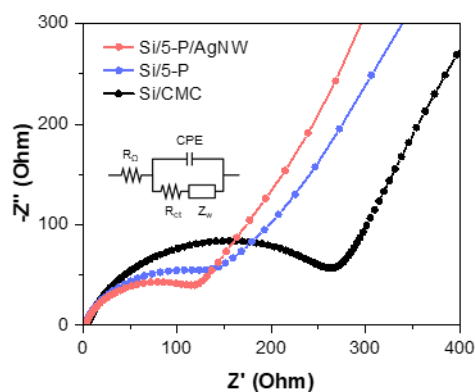


Figure 20. Nyquist plots of different electrodes after 20 cycles of charge/discharge. The inset is an equivalent circuit model.

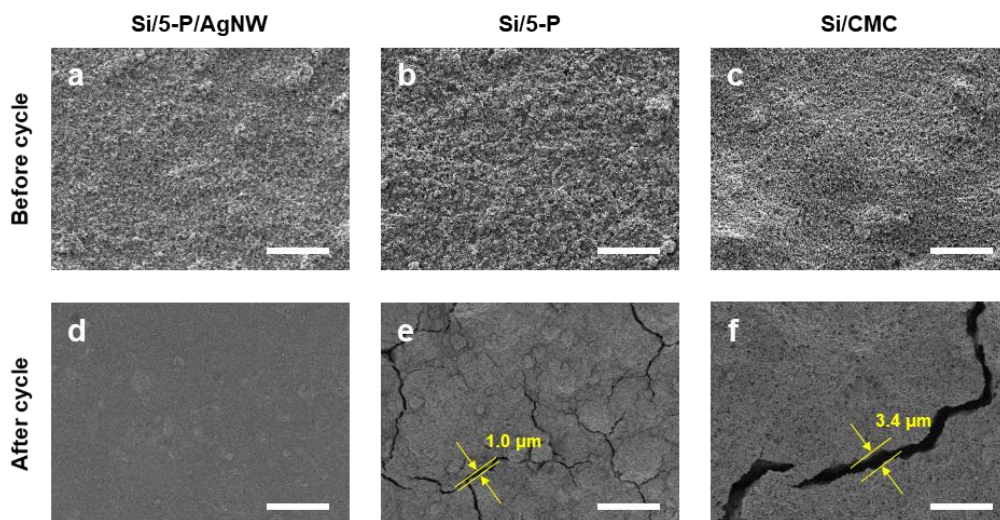


Figure 21. SEM images of the electrode surface (a-c) before and (d-e) after charge/discharge cycles. (a), (d) Si/5-P/AgNW, (b), (e) Si/5-P, and (c), (f) Si/CMC electrodes. The scale bars are 10 μm .

Chapter 5. Conclusion

5.1. Summary of this work

In this paper, conductive polymer composites with chain length-induced hierarchical structures are fabricated as a binder for Si anodes in LIBs. It attains prominent improvements in electrical conductivity (~40%) and stretchability (~60%) compared to conductive polymer composites with PEG or PEO, which are critical factors for preventing electrical contact loss and delamination of SiNPs. Moreover, AgNWs that are added to Si anodes with low mass loading (~5wt%) successfully form 3D entangled networks, imparting superior electron paths, sufficient void space for huge volume changes, and highly adhesive interaction with the Cu foil current collector. Si/5-P/AgNW electrode shows higher specific capacity (1066 mAh g⁻¹) than Si/5-P (830 mAh g⁻¹) and Si/CMC electrodes (128 mAh g⁻¹) under the current density of 0.8 A g⁻¹ after 100 cycles. Improved performance of Si/5-P/AgNW electrode is reconfirmed with low charge transport resistance and rare cracks during repeated charge/discharge cycles.

5.2. Future work

Conductive polymers with hierarchical structures and AgNW network are employed and achieve improvements in electrical, mechanical, and electrochemical performances. Firstly, the combined effect of PEO and PEG that have different molecular weights can be applied to other conventional binders to offer evenly distributed ether groups that are capable of improving reversible stretchability and ionic conductivity for Li-ion. Second, not only PEG and PEO, polymers with the

same monomer unit and different molecular weights would be used for constructing hierarchical structures, imparting various functions to the polymer. Last but not least, 3D entangled network in the electrode is found highly promising in that it naturally makes buffer space for volume changes of active materials and prevents delamination of electrode materials by enhancing adhesions to the current collector. Therefore, randomly distributed 1D materials that can reversibly react with Li are expected to enhance the structural stability of electrodes while attaining high electrochemical performance for cathodes and anodes in LIBs.

Reference

1. Bollen, M. H. J.; Ronnberg, S. K., Hosting Capacity of the Power Grid for Renewable Electricity Production and New Large Consumption Equipment. *Energies* **2017**, *10* (9), 1325.
2. Sensfuß, F.; Ragwitz, M.; Genoese, M., The merit-order effect: A detailed analysis of the price effect of renewable electricity generation on spot market prices in Germany. *Energy policy* **2008**, *36* (8), 3086-3094.
3. Shakya, S. R.; Shrestha, R. M., Transport sector electrification in a hydropower resource rich developing country: Energy security, environmental and climate change co-benefits. *Energy for Sustainable Development* **2011**, *15* (2), 147-159.
4. Singh, B.; Stromman, A. H., Environmental assessment of electrification of road transport in Norway: Scenarios and impacts. *Transportation Research Part D-Transport and Environment* **2013**, *25*, 106-111.
5. Manzetti, S.; Mariasiu, F., Electric vehicle battery technologies: From present state to future systems. *Renewable & Sustainable Energy Reviews* **2015**, *51*, 1004-1012.
6. Fotouhi, A.; Auger, D. J.; Propp, K.; Longo, S.; Wild, M., A review on electric vehicle battery modelling: From Lithium-ion toward Lithium-Sulphur. *Renewable & Sustainable Energy Reviews* **2016**, *56*, 1008-1021.
7. Ebrahimi, S.; Mac Kinnon, M.; Brouwer, J., California end-use electrification impacts on carbon neutrality and clean air. *Applied Energy* **2018**, *213*, 435-449.
8. Zuo, X. X.; Zhu, J.; Muller-Buschbaum, P.; Cheng, Y. J., Silicon based lithium-ion battery anodes: A chronicle perspective review. *Nano Energy* **2017**, *31*, 113-143.
9. Su, X.; Wu, Q. L.; Li, J. C.; Xiao, X. C.; Lott, A.; Lu, W. Q.; Sheldon, B. W.; Wu, J., Silicon-Based Nanomaterials for Lithium-Ion Batteries: A Review. *Advanced Energy Materials* **2014**, *4* (1), 1300882.
10. Choi, J. W.; Aurbach, D., Promise and reality of post-lithium-ion batteries with high energy densities. *Nature Reviews Materials* **2016**, *1* (4), 1-16.
11. Ge, M.; Rong, J.; Fang, X.; Zhou, C., Porous doped silicon nanowires for lithium ion battery anode with long cycle life. *Nano Lett* **2012**, *12* (5), 2318-23.
12. Ryu, J.; Hong, D.; Choi, S.; Park, S., Synthesis of Ultrathin Si Nanosheets from Natural Clays for Lithium-Ion Battery Anodes. *ACS Nano* **2016**, *10* (2), 2843-51.
13. Wu, J. X.; Qin, X. Y.; Zhang, H. R.; He, Y. B.; Li, B. H.; Ke, L.; Lv, W.; Du, H. D.; Yang, Q. H.; Kang, F. Y., Multilayered silicon embedded porous carbon/graphene hybrid film as a high performance anode. *Carbon* **2015**, *84*, 434-443.
14. Liu, T. F.; Chu, Q. L.; Yan, C.; Zhang, S. Q.; Lin, Z.; Lu, J., Interweaving 3D Network Binder for High-Areal-Capacity Si Anode through Combined Hard and Soft Polymers. *Advanced Energy Materials* **2019**, *9* (3), 1802645.
15. Yue, L.; Zhang, L. Z.; Zhong, H. X., Carboxymethyl chitosan: A new water soluble binder for Si anode of Li-ion batteries. *Journal of Power Sources* **2014**, *247*, 327-331.
16. Liu, J.; Zhang, Q.; Wu, Z. Y.; Wu, J. H.; Li, J. T.; Huang, L.; Sun, S. G., A

high-performance alginate hydrogel binder for the Si/C anode of a Li-ion battery. *Chem Commun (Camb)* **2014**, 50 (48), 6386-9.

17. Magasinski, A.; Zdyrko, B.; Kovalenko, I.; Hertzberg, B.; Burtovyy, R.; Huebner, C. F.; Fuller, T. F.; Luzinov, I.; Yushin, G., Toward efficient binders for Li-ion battery Si-based anodes: polyacrylic acid. *ACS Appl Mater Interfaces* **2010**, 2 (11), 3004-10.

18. Zhang, H. R.; Qin, X. Y.; Wu, J. X.; He, Y. B.; Du, H. D.; Li, B. H.; Kang, F. Y., Electrospun core-shell silicon/carbon fibers with an internal honeycomb-like conductive carbon framework as an anode for lithium ion batteries. *Journal of Materials Chemistry A* **2015**, 3 (13), 7112-7120.

19. Yao, Y.; Liu, N.; McDowell, M. T.; Pasta, M.; Cui, Y., Improving the cycling stability of silicon nanowire anodes with conducting polymer coatings. *Energy & Environmental Science* **2012**, 5 (7), 7927-7930.

20. Kummer, M.; Badillo, J.; Schmitz, A.; Bremes, H.-G.; Winter, M.; Schulz, C.; Wiggers, H., Silicon/polyaniline nanocomposites as anode material for lithium ion batteries. *Journal of the Electrochemical Society* **2013**, 161 (1), A40.

21. Shi, H.; Liu, C. C.; Jiang, Q. L.; Xu, J. K., Effective Approaches to Improve the Electrical Conductivity of PEDOT:PSS: A Review. *Advanced Electronic Materials* **2015**, 1 (4), 1500017.

22. Dong, J. J.; Portale, G., Role of the Processing Solvent on the Electrical Conductivity of PEDOT:PSS. *Advanced Materials Interfaces* **2020**, 7 (18), 2000641.

23. Zeng, W. W.; Wang, L.; Peng, X.; Liu, T. F.; Jiang, Y. Y.; Qin, F.; Hu, L.; Chu, P. K.; Huo, K. F.; Zhou, Y. H., Enhanced Ion Conductivity in Conducting Polymer Binder for High-Performance Silicon Anodes in Advanced Lithium-Ion Batteries. *Advanced Energy Materials* **2018**, 8 (11), 1702314.

24. Higgins, T. M.; Park, S. H.; King, P. J.; Zhang, C.; MoEvoy, N.; Berner, N. C.; Daly, D.; Shmeliov, A.; Khan, U.; Duesberg, G.; Nicolosi, V.; Coleman, J. N., A Commercial Conducting Polymer as Both Binder and Conductive Additive for Silicon Nanoparticle-Based Lithium-Ion Battery Negative Electrodes. *Acs Nano* **2016**, 10 (3), 3702-3713.

25. Bang, J.; Coskun, S.; Pyun, K. R.; Doganay, D.; Tunca, S.; Koylan, S.; Kim, D.; Unalan, H. E.; Ko, S. H., Advances in protective layer-coating on metal nanowires with enhanced stability and their applications. *Applied Materials Today* **2021**, 22, 100909.

26. Jung, J.; Cho, H.; Yuksel, R.; Kim, D.; Lee, H.; Kwon, J.; Lee, P.; Yeo, J.; Hong, S.; Unalan, H. E.; Han, S.; Ko, S. H., Stretchable/flexible silver nanowire Electrodes for energy device applications. *Nanoscale* **2019**, 11 (43), 20356-20378.

27. Youn, D.-Y.; Kim, C.; Cheong, J. Y.; Cho, S.-H.; Yoon, K. R.; Jung, J.-W.; Kim, N.-H.; Kim, I.-D., Stable and High-Capacity Si Electrodes with Free-Standing Architecture for Lithium-Ion Batteries. *ACS Applied Energy Materials* **2019**, 3 (1), 208-217.

28. Lu, L. L.; Ge, J.; Yang, J. N.; Chen, S. M.; Yao, H. B.; Zhou, F.; Yu, S. H., Free-Standing Copper Nanowire Network Current Collector for Improving Lithium Anode Performance. *Nano Lett* **2016**, 16 (7), 4431-7.

29. Wei, D. F.; Mao, J.; Zheng, Z. A.; Fang, J. J.; Luo, Y. W.; Gao, X., Achieving a high loading Si anode via employing a triblock copolymer elastomer binder, metal nanowires and a laminated conductive structure. *Journal of Materials Chemistry A* **2018**, 6 (42), 20982-20991.

30. Won, P.; Park, J. J.; Lee, T.; Ha, I.; Han, S.; Choi, M.; Lee, J.; Hong, S.; Cho, K. J.; Ko, S. H., Stretchable and Transparent Kirigami Conductor of Nanowire Percolation Network for Electronic Skin Applications. *Nano Lett* **2019**, *19* (9), 6087-6096.
31. Nguyen, T. P.; Le Rendu, P.; Long, P. D.; De Vos, S. A., Chemical and thermal treatment of PEDOT : PSS thin films for use in organic light emitting diodes. *Surface & Coatings Technology* **2004**, *180*, 646-649.
32. Lin, Y.-J.; Ni, W.-S.; Lee, J.-Y., Effect of incorporation of ethylene glycol into PEDOT: PSS on electron phonon coupling and conductivity. *Journal of Applied Physics* **2015**, *117* (21), 215501.
33. Maxfield, J.; Shepherd, I., Conformation of poly (ethylene oxide) in the solid state, melt and solution measured by Raman scattering. *Polymer* **1975**, *16* (7), 505-509.
34. Prosanov, I. Y.; Matvienko, A. A., Study of PVA thermal destruction by means of IR and Raman spectroscopy. *Physics of the Solid State* **2010**, *52* (10), 2203-2206.
35. Huang, T. M.; Batra, S.; Hu, J. H.; Miyoshi, T.; Cakmak, M., Chemical cross-linking of conducting poly(3,4-ethylenedioxythiophene):poly(styrenesulfonate) (PEDOT:PSS) using poly(ethylene oxide) (PEO). *Polymer* **2013**, *54* (23), 6455-6462.
36. Ghiji, M.; Novozhilov, V.; Moinuddin, K.; Joseph, P.; Burch, I.; Suendermann, B.; Gamble, G., A Review of Lithium-Ion Battery Fire Suppression. *Energies* **2020**, *13* (19), 5117.
37. Pace, C. N.; Fu, H.; Lee Fryar, K.; Landua, J.; Trevino, S. R.; Schell, D.; Thurlkill, R. L.; Imura, S.; Scholtz, J. M.; Gajiwala, K.; Sevcik, J.; Urbanikova, L.; Myers, J. K.; Takano, K.; Hebert, E. J.; Shirley, B. A.; Grimsley, G. R., Contribution of hydrogen bonds to protein stability. *Protein Sci* **2014**, *23* (5), 652-61.
38. Herth, E.; Zeggari, R.; Rauch, J. Y.; Remy-Martin, F.; Boireau, W., Investigation of amorphous SiO_x layer on gold surface for Surface Plasmon Resonance measurements. *Microelectronic Engineering* **2016**, *163*, 43-48.
39. Lawes, S.; Sun, Q.; Lushington, A.; Xiao, B. W.; Liu, Y. L.; Sun, X. L., Inkjet-printed silicon as high performance anodes for Li-ion batteries. *Nano Energy* **2017**, *36*, 313-321.
40. Goudarzi, M.; Mir, N.; Mousavi-Kamazani, M.; Bagheri, S.; Salavati-Niasari, M., Biosynthesis and characterization of silver nanoparticles prepared from two novel natural precursors by facile thermal decomposition methods. *Sci Rep* **2016**, *6* (1), 32539.
41. Hu, S. M.; Wang, L. D. Y.; Huang, T.; Yu, A. S., A conductive self-healing hydrogel binder for high-performance silicon anodes in lithium-ion batteries. *Journal of Power Sources* **2020**, *449*, 227472.
42. Xie, Z. H.; Rong, M. Z.; Zhang, M. Q., Dynamically Cross-Linked Polymeric Binder-Made Durable Silicon Anode of a Wide Operating Temperature Li-Ion Battery. *ACS Appl Mater Interfaces* **2021**, *13* (24), 28737-28748.

국문 초록

리튬이온 배터리 실리콘 음극을 위한 금속 나노와이어 도전재 및 상이 사슬 길이 구조 기반 전도성 고분자 바인더 개발

김재원

기계공학부

서울대학교 대학원

실리콘은 리튬 이온 배터리의 차세대 음극재로 주목받는 물질로, 기존의 흑연 대비 매우 높은 충전 용량을 가진다. 하지만 충·방전시 급격한 부피 변화로 충전 용량이 급격히 감소하는 것이 난제이다. 본 연구에서는 상이 사슬 길이를 이용한 계층 구조 기반 전도성 고분자 바인더를 개발하였다. 계층 구조를 통해 균일하고 밀집된 수소 결합 및 가교 다발을 형성하여 다른 전도성 고분자 대비 높은 전기적 전도성과 인장 길이를 보여주었다. 이에 더해, 은 나노와이어 네트워크를 이용하여 3D 전기적 연결 강화, 부피 변화 완충을 위한 다공성 확보, 그리고 집전 장치와의 접촉성 향상을 달성하였다. 전도성 바인더와 은 나노와이어 네트워크를 활용하여 제작된 음극은 전류 밀도 0.8 A g^{-1} 의 충·방전 100번째 사이클에서 1066 mAh g^{-1} 의 높은 전하 용량을 달성하며, 다른 종류의 음극 대비 우수한 용량 및 수명 특성을 보여주었다. 또한, 주사전자현미경과 전기화학적 임피던스 분광 기법을 활용하여 각각 실리콘 입자 부피 완충 능력과 전자 교환 특성이 향상되었음을 확인하였다.

주요어 : 리튬이온 배터리, 실리콘 음극, 전도성 바인더, 계층 구조, 은 나노와이어

학 번 : 2020-27003